Journal of Southeast University (English Edition) Vol. 36, No. 4, pp. 414 – 424 Dec. 2020 ISSN 1003—7985

Flexural behaviour of SFRRAC two-way composite slab with different shapes

Luo Bin[1] Huang Wei[2]

([1]School of Civil Engineering, Lanzhou University of Technology, Lanzhou 730050, China)
([2]School of Civil Engineering, Xi'an University of Architecture and Technology, Xi'an 710055, China)

Abstract: To promote the application of green renewable materials in concrete composite slabs (CCSs) and study the flexural behavior of CCSs with different shapes, the bending performances of three CCSs with a SFRRAC base plate, one cast-in-site concrete slab of ordinary concrete and one CCS of ordinary concrete by steel bar truss (as recommended in the technical specification for precast concrete structures in Chinese) were compared through experiments. The carrying capacity, flexural behaviour and bi-directional mechanical properties of the specimens were systematically analyzed from the failure modes, load-deflection curves, load-bar strain curves, load-slip curves and crack distributions. Results show that the bending failure process of CCSs with a SFRRAC base plate is similar to that of the cast-in-site concrete slab of ordinary concrete and CCS of ordinary concrete by steel bar truss, as all of them went through the plastic phase, elastic plastic phase and failure phase with fully developed cracks and deflection. No sudden breakage or horizontal cracking of the connecting interface between the base plate and concrete topping was observed. The shape of the base plate has a major impact on the bearing capacity of the CCS with the SFRRAC base plate. When calculating the ultimate bearing capacity with the plastic yield line theory, the influence of the base plate shape on the plastic yield line position should be taken into account.

Key words: concrete composite slab (CCS); shape; steel bar truss; bending performance; ultimate bearing capacity
DOI: 10.3969/j.issn.1003 – 7985.2020.04.007

The precast concrete structure has the advantages of being labour-saving, energy-efficient and having low-carbon features[1]. It will be widely used in residential construction. One of the key components of this structure is the concrete composite slab (CCS), which supports the fast construction of solid buildings with a few templates[2–4]. With the proliferation of the precast concrete structure, the CCS has been widely applied in residential construction across China and elsewhere in the world.

Much theoretical research has been done on the design, production and construction of the CCS, yielding various CSSs that are easy to transport and install. For instance, Mohammed et al.[5–6] developed a CCS by adopting crumb rubber fine aggregates in the concrete topping, creating a solution for the disposal of waste tires. Majdi et al.[7] put forward a CSS with a bottom of cold-formed steel profiles, corrugated steel decks, a concrete topping and furring channels, which maximizes the advantages and minimizes the disadvantages of steel and concrete. An et al.[8] proposed an innovative cable supported beam structure-concrete slab composite floor. Kim et al.[9] designed a CCS with concrete, steel bars, perfobond rib shear connectors, and profiled steel sheets vertical to the girder, aiming to create a large interior space required for public buildings and bridges. Ueda et al.[10–11] presented several types of precast hollow CCSs to overcome the heavy weight and transportation difficulty of the ferrocement-brick composite slab created by Thanoon et al[12]. Carbonari et al.[13–15] proposed precast concrete sandwich panels in different forms and with different materials, in an attempt to preserve the heat and integrate the load bearing capacities of precast components; and the feasibility of these panels were verified through calculation by Benayoune's theory[16]. All of the above studies have contributed greatly to the development of the CSS and reflect the local conditions of various application scenarios.

The rapid urbanization in China is accompanied by an upsurge in the amount of construction wastes (about 30% to 40% of urban wastes), posing a serious threat to ecological environments[17]. To mitigate the threat, a viable option lies in the preparation of green concrete through recycling of the huge amount of construction wastes[18]. In this way, it is possible to produce recycled aggregate concrete from recycled aggregates instead of natural aggregates, and apply it in the industrial production of precast concrete structure components like the CCS. This approach will relieve the excessive consumption of concrete, reduce the pollution from construction wastes, and match with the trend of construction industrialization and green buildings.

Nevertheless, ordinary aggregate concrete is often out-

Received 2020-05-23, **Revised** 2020-09-27.

Biographies: Luo Bin (1985—), male, doctor, lecturer; Huang Wei (corresponding author), male, doctor, professor, huanwei2005@126.com.

Foundation item: The National Natural Science Foundation of China (No. 51578446).

Citation: Luo Bin, Huang Wei. Flexural behaviour of SFRRAC two-way composite slab with different shapes[J]. Journal of Southeast University (English Edition), 2020, 36(4): 414 – 424. DOI: 10.3969/j.issn.1003 – 7985.2020.04.007.

performed by the recycled aggregate concretes, owing to the latter's low apparent density, internal micro-cracks and high crush index, leading to a limited application for engineering[19]. In previous studies, our research groups have introduced steel fibres into recycled aggregate concrete to enhance the apparent density and reduce internal micro-cracks creating the steel fibre-reinforced recycled aggregate concrete (SFRRAC)[20], and proved that the steel fibres can effectively prevent the micro-crack development and improve the mechanical performance of recycled aggregate concrete.

Inspired by the research results on the SFRRAC, this paper combines the SFRRAC base plates of three different shapes with cast-in-situ concrete topping into CCSs, with the aim to developing CCSs with excellent mechanical properties. Five full-scale specimens were produced, including three SFRRAC CCSs of different shapes, one cast-in-situ concrete slab, and one ordinary concrete CCS reinforced by steel bar truss according to the Chinese technical specification JGJ 1—2014[21]. Finally, the authors derived the calculation formula of the ultimate bearing capacity of the SFRRAC CCSs.

1 Experimental Program

1.1 Details of specimens

Five specimens, denoted as S1 to S5, were designed according to the dimensions and parameters in Tab. 1 and Fig. 1(a), of which S1 and S2 are control specimens. S1 is the cast-in-site concrete specimen, and S2 to S5 are CCS specimens. S2 to S5 consist of a precast base plate and a cast-in-site concrete topping. S2 to S5 share the same topping (ordinary concrete) and differ in the precast base plate. S2 has ordinary concrete base plates, while S3 to S5 have SFRRAC base plates. In Tab. 1, L is the span of the specimen, W is the width of the specimen, t_b is the thickness of precast panel, and t_t is the thickness of cast-in-site concrete topping (or the thickness of cast-in-site).

In addition, the precast base plates of the five specimens were equipped with two-way (i.e. X-/Y- direction) reinforcements, which adopted eight hot rolled ribbed bars $D8$ (diameter 8 mm) spaced at 150 mm ($D8@150$). In order to prevent cracking during hoisting, 6 mm-diameter hot rolled plan bars $D6$ spaced at 250 mm ($D6@250$) used as transverse reinforcement were arranged on the top of all specimens. Meanwhile, the A90 type steel bar truss was used for the Y-direction of four precast base plates of S2, S3, S4, S5, and the A70 type steel bar truss was used for the X-direction of precast base plate of S4. Details of specimens reinforcement are shown in Fig. 1(b).

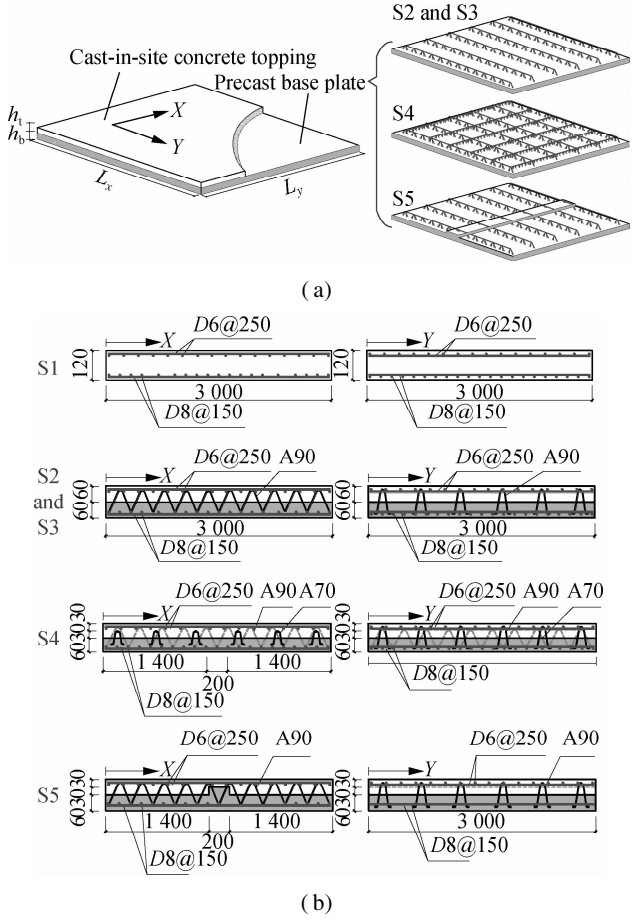

Fig. 1 The structure and reinforcements of the specimens. (a) Shape of CCSs; (b) Cross section of specimens

Tab. 1 Basic parameters of specimens

No.	Precast base plate			Material of cast-in-site concrete topping (or cast-in-site of S1)	$L_x \times L_y \times t_b \times t_t$/ (mm × mm × mm × mm)	Type of slabs
	Type of shape		Kind of material			
	X-direction	Y-direction				
S1				Ordinary concrete	3000 × 3000 × 0 × 120	Cast-in-site
S2		Steel bar truss	Ordinary concrete	Ordinary concrete	3000 × 3000 × 60 × 60	CCS
S3		Steel bar truss	SFRRAC	Ordinary concrete	3000 × 3000 × 60 × 60	CCS
S4	Steel bar truss	Steel bar truss	SFRRAC	Ordinary concrete	3000 × 3000 × 60 × 60	CCS
S5	Steel bar truss	Rectangular-rib	SFRRAC	Ordinary concrete	3000 × 3000 × 60 × 60	CCS

Note: The rib height is 30 mm and the rib width is 200 mm in the rectangular rib.

1.2 Properties of specimens

According to the our previous research[20], the raw materials of the SFRRAC precast base plates were selected: All coarse aggregates were crushed and screened waste concretes; the fine aggregates were natural sand; the steel fibres (volume fraction 1%; length 35 mm; diameter 0.56 mm; tensile strength 2 300 MPa) were shear-pattern

steel fibres.

Three cubes (side length 150 mm) and three prisms ($L \times W \times H = 150$ mm $\times$ 150 mm $\times$ 300 mm) were prepared for each specimen to measure the actual cubic compressive strength, splitting tensile strength and axial compressive strength (see Tab. 2)[22]. The mechanical properties of the reinforcements are listed in Tab. 3.

Tab. 2 Mechanical properties of concretes

Material	Position	Cubic compressive strength f_{cu} or f_{fcu}/MPa	Axial compressive strength f_c/MPa	Splitting tensile strength f_{ts}/MPa	Elastic modulus/GPa
Ordinary concrete	Precast bottom panel	34.9	25.7	3.12	31.3
SFRRAC	Precast bottom panel	37.5	30.5	3.78	32.0
Ordinary concrete	Cast-in-site concrete topping	35.8	27.3	3.14	31.6

Note: The elastic modulus in the table is calculated according to the calculation method of 4.0.2 in the Standard Test Method for Concrete Structures (GB/T 50152—2012)[23].

Tab. 3 Mechanical properties of reinforcement

Type	Diameter/mm	Yield strength/MPa	Ultimate strength/MPa	Elastic modulus/GPa
Hot rolled ribbed bars	6	310	398	210
Hot rolled ribbed bars	8	410	598	200

1.3 Fabrication process of specimens

Each of the four CCS specimens was fabricated in two stages. As shown in Fig. 2(a), the precast base plate was produced through mould fixing, brushing of the release agent, bar bindings, concrete pouring, and surface roughening. As shown in Fig. 2(b), the cast-in-site concrete topping was fabricated after the concrete strength of the base plate reached 100% through the following steps: mould fixing, bar bindings, and concrete pouring.

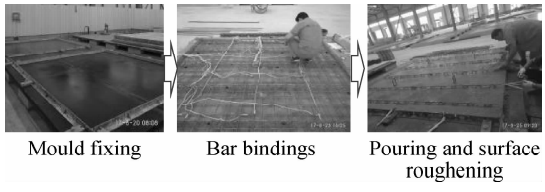

(a)

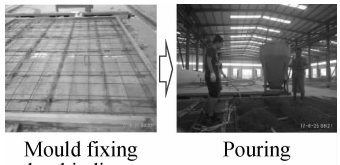

(b)

Fig. 2 Construction procedure of specimens. (a) Precast bottom panel; (b) Cast-in-site concrete topping

1.4 Test setup and procedure

During the experiment, the load was applied manually via a 1 000 kN hydraulic actuator. Each slab was simply supported on four sides and subjected to the load at eight points in the *Y*-direction and four points in the *X*-direction. All points were under the same load, creating a homogenous loading pattern. The force generated by the hydraulic pump was transferred from the jack to the specimen via rigid girders. To prevent punching failure, a square steel pad with a side length of 200 mm was placed under the second rigid girder, and covered with sand at its bottom. The experimental set-up is shown in Fig. 3.

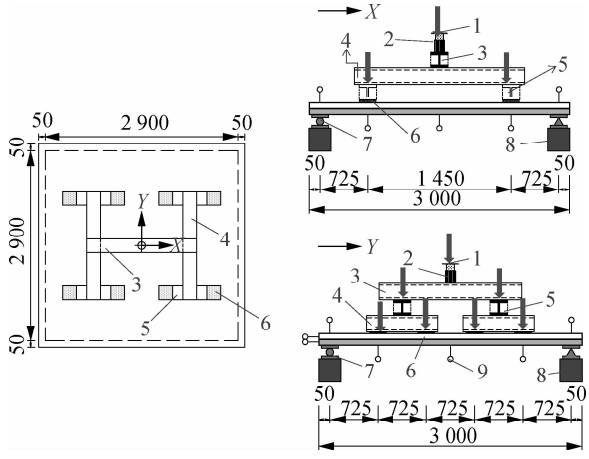

1—sensor; 2—jack; 3—first stage distribution beam; 4—second stage distribution beam; 5—third stage distribution beam; 6—steel pad; 7—support; 8—specimen's bracket; 9—LVDTs

(a)

(b)

Fig. 3 Test loading. (a) Loading devices and testing instruments (unit: mm); (b) Typical test photograph

According to the Chinese standard GB/T 50152—2012[23], the loading process was divided into pre-loading and formal loading. In pre-loading, there were three loading phases and three unloading phases, each of which had a load increment of 5 kN. In formal loading, the load increment was initially 5 kN per phase, adjusted to 10 kN per phase after the cracking of the specimen, and changed back to 5 kN per phase when the load reached 90% of the calculated ultimate bearing capacity. After each load increment, the mid-span deflection, strain and crack propagation pattern were recorded for further analysis.

It is considered that the specimen has reached the limit state of bearing capacity and stopped loading[23], when the specimen reaches one of the following conditions: The midspan deflection reaches 1/50 of the full span, the crack width of the slab bottom concrete widens to 1.50 mm, the strain of steel bar reaches 0.01, and the concrete is crushed in the compressive zone or the fracture of tension reinforcement.

1.5 Measurements

The vertical load was measured by the force sensor in Fig. 4(a). A total of five linear variable displacement transducers (LVDTs) were placed at the bottom of each specimen to measure the bending deflection in two directions(i.e. W2, W3, W4, W7, and W8), and four LVDTs were placed at the top of each specimen(i.e. W1, W5, W6, W9). Two LVDTs were arranged, respectively, at the two ends of the precast base plate and concrete topping to record the interface slip(i.e. W10 and W11). As shown in Fig. 4(b), eighteen bar strain gauges were installed on the compressive bar in *X*-directions (i.e. X_1 to X_9) and *Y*-directions (i.e. Y_1 to Y_9) on specimen bottom. A steel bar strain gauge was provided at the upper/ lower chords and web of the bar closest to the slab centre of the steel bar truss in specimens(S2 to S5).

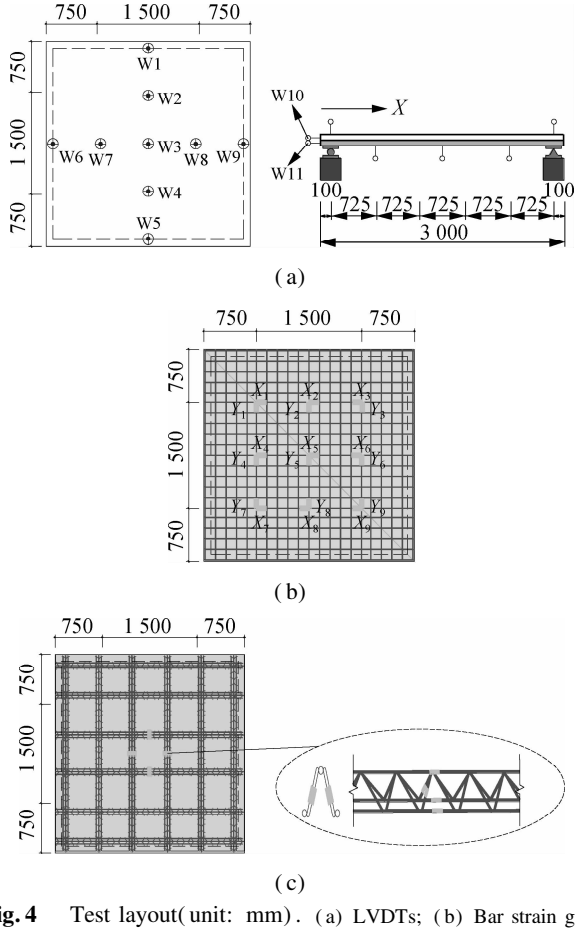

Fig. 4 Test layout(unit: mm). (a) LVDTs; (b) Bar strain gauges of reinforcements; (c) Bar strain gauges of steel bar truss

1.6 Characteristic load determination method

The cracking load was determined in three ways: Firstly, when the first crack appears in the loading process, the corresponding load should be taken as the cracking load; secondly, when the first crack appears in a specific loading phase, the mean load between the current phase and the previous phase should be taken as the cracking load; thirdly, when the first crack appears after a specific loading phase, the current load should be taken as the cracking load[23].

The yield load of a member was determined by the farthest point method[24], that is, the yield load of a member should be measured at the yield point whose tangent slope is the same as the connecting line between the origin and the ultimate loading point. The yield point determination is detailed in Fig. 5. The calculation method of the yield point load is shown as

$$(F_{ys}, D_{ys}) = \max_{(F_{ys}, D_{ys}) = (F, D)} d = \frac{|F_p D - D_p F|}{\sqrt{F_p^2 + D_p^2}} \quad (1)$$

where (F, D) is the component of the force-deformation curve; (F_{ys}, D_{ys}) is the yield point coordinate obtained by the farthest point method; and (F_p, D_p) is the peak point coordinate $(0 \leqslant D \leqslant D_p)$.

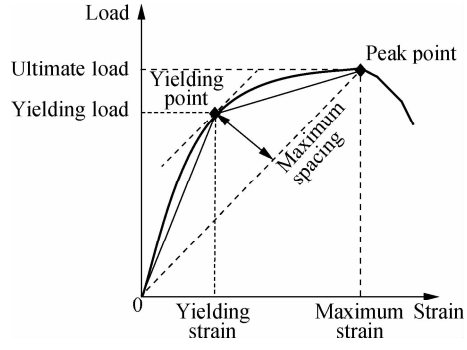

Fig. 5 Proposed method for determining the yielding point

2 Test Results and Discussion

2.1 Failure modes and crack pattern

The following phenomena can be observed from the failure patterns of the five specimens as shown in Fig. 6.

1) Throughout the experiment, the five specimens had similar responses to the external load, all of which went through the elastic deformation, concrete cracking, upward crack propagation, compressive bar yielding, continuous crack extension, and corner warpage. Ultimately, the specimens failed under deflection as the cracking exceeded the maximum limit, and exhibited a "butterfly" deformation pattern. There was neither shear failure inside the slab nor local punching failure at the pad. However, it is noteworthy that S2, S3 and S5 had much added distribution of cracks in the *X*-direction than in the *Y*-

direction at the mid-span of the slab, although the final cracks of all specimens were plastic yield lines exhibiting an "X" pattern. This is attributed to the shape difference of the precast base plate in the two directions and can be explained by the concept of the orthotropic reinforcement slab in Ref. [25].

2) Specimens with different base plate materials (S2 vs. S3) are compared. When the specimens reached the cracking load, it was observed that S2 had fewer cracks than S3, but its bottom and sides were much less cracked than those of S3 near the end of the elastic-plastic phase. A possible reason can be found in Ref. [26]. When specimens were subjected to a small load, the steel fibres in the matrix hindered the expansion of cracks in the concrete, enhancing the crack resistance of brittle matrix material under bi-directional tension. In the later phase of loading, however, steel fibres were broken and even pulled out, as the anchorage length in the base concrete became insufficient.

3) Specimens in different shapes (S3 vs. S4 vs. S5 are compared). Throughout the loading process, our specimens neither exhibited any adhesion failure at the interface between the bottom plate and the concrete top, nor separation between the two components on the slab side (as evidenced by the load-slip curves in Section 2.5). This means that all the CCS shapes in our experiment ensure a good coordination between the base plate and the concrete topping.

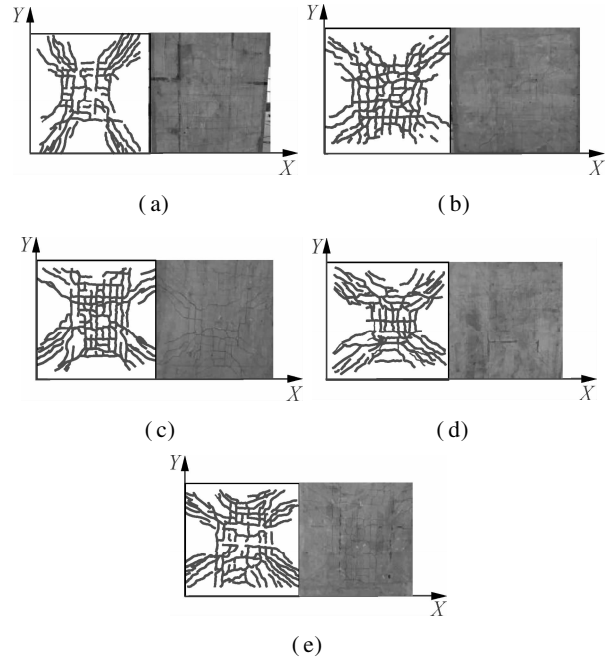

Fig. 6 Ultimate failure pattern of composite slab. (a) S1; (b) S2; (c) S3; (d) S4; (e) S5

2.2 Carrying capacity

Fig. 7 presents the cracking load P_{cr}, yielding load P_y and ultimate load P_u measured in the experiment. The load value of 78.12 kN was calculated by Load Code for the Design of Building Structures (GB 50009—2012); i.e., the variable load value was 2.0 kN/m^2, and a value of 4.9 kN/m^2 was the permanent load value after taking into account the architectural practice.

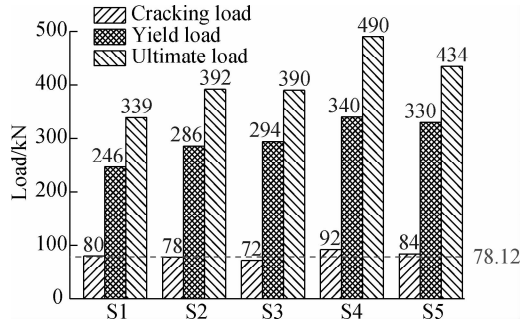

Fig. 7 Characteristic load values of the specimens

1) S1 vs. S2 to S5. The five specimens displayed high load bearing capacities, which satisfied the load bearing requirements for residential buildings in the Chinese standard GB 50009—2012[27]. The ultimate loads of S2, S3, S4 and S5 were, respectively, 15.63%, 15.04%, 44.54% and 28.02% higher than the ultimate load of S1. This is because the load bearing capacity of the cast-in-situ concrete slab can be easily outweighed if the CCS has a rational shape, despite the connecting interface between the precast base plate and the concrete topping.

2) S2 vs. S3. The two specimens shared similar cracking loads, yielding loads and ultimate loads, indicating that the SFRRAC base plate can satisfy the load bearing requirements for the CCS in the Chinese standard JGJ 1—2014[21].

3) S3 vs. S4 vs. S5. The cracking load, yielding load and ultimate load of S3 were 27.77%, 15.65% and 25.64% lower than S4 and 16.67%, 12.24% and 11.28% lower than S5, respectively. This reveals that the bi-direction reinforcement of the precast bottom panel can enhance the load bearing capacity of the connecting interface. After all, each slab specimen had to withstand loads in both directions[28]: $\frac{\partial^2 m_x}{\partial x^4} + 2\frac{\partial^4 m_{xy}}{\partial_x \partial_y} + \frac{\partial^2 m_y}{\partial y^2} = -q.$ In addition, the steel bar truss can improve the load bearing capacity, especially the ultimate bearing capacity, of the CCS more significantly than the rectangular rib. This is because the load on the compressive bars at the bottom of each cracked specimen is partially carried by the top/bottom chords and web members.

2.3 Deflection and ductility

2.3.1 Load-deflection curves

The mid-span load-deflection (F-δ) curves of our specimens are presented in Fig. 8. The ductility index, i.e. the ratio of the ultimate deflection to the deflection at the yielding of compressive bars[29], is shown in Tab. 4.

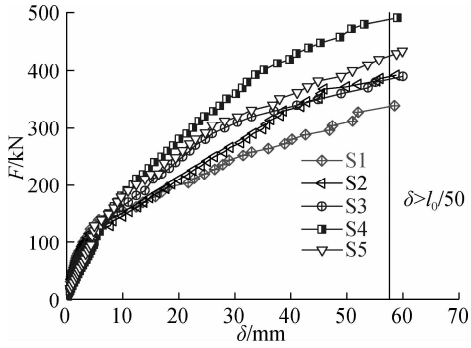

Fig. 8 Load-deflection curves at mid-span

Tab. 4 Ductility of the specimens

No.	Displacement at yield load/mm	Displacement at ultimate load/mm	Ductility factor
S1	29.00	58.50	2.02
S2	31.35	58.80	1.88
S3	30.56	60.00	1.96
S4	27.86	59.00	2.11
S5	32.35	59.89	1.85

1) S1 vs. S2 to S5. Similar trends can be observed from the load-deflection curves of the five specimens in the experiment. The curves were approximately straight lines at the beginning of loading and became nonlinear after the concrete cracked. Moreover, the line segment of each curve between the elastic-plastic phase and the failure phase was very long and the ductility index had a high value, which signify the good ductility and bending performance of all specimens. Unlike the uni-directional CCSs in Refs. [30 − 32], the curves of our specimens always maintained a growing trend until the end of loading, due to the tensile membrane effect in the later phase of the bi-directional reinforcement.

2) S2 vs. S3. As steel fibers can inhibit concrete cracking, the slope of curve S3 was larger at the early stage of the elastic phase and the elastic-plastic phase than that of S2. Meanwhile, the slope of the S3 curve decreased faster than that of the S2 curve, as the steel fibres were pulled out from the bidirectional tensile zone at the bottom under the continuously growing load in the elastic-plastic phase. This is consistent with the experimental phenomenon mentioned in Section 2.1.

3) S3 vs. S4 vs. S5. In the later phase of loading, S4 had the lowest deflection under the same load. The ductility index of S4 was 7.60% and 14.05%, respectively, higher than those of S3 and S5. Therefore, the CCS were enhanced with steel bar truss in both the *X*- and *Y*-directions can boost the load bearing capacity and enhance subsequent stiffness and ductility.

2.3.2 Flexural performance of two-way

The deflections δ of each specimen at different positions in the *X* (W6, W7, W3, W8, W9)- and *Y* (W1, W2, W3, W4, W5)-directions were recorded by the LVDTs in Fig. 4(a) and plotted into curves in Fig. 9.

1) S1 vs. S2 to S5. Under the same load level, the vertical displacement was negatively correlated with the distance between the measuring point and the slab centre. The curves all changed into a parabolic shape under

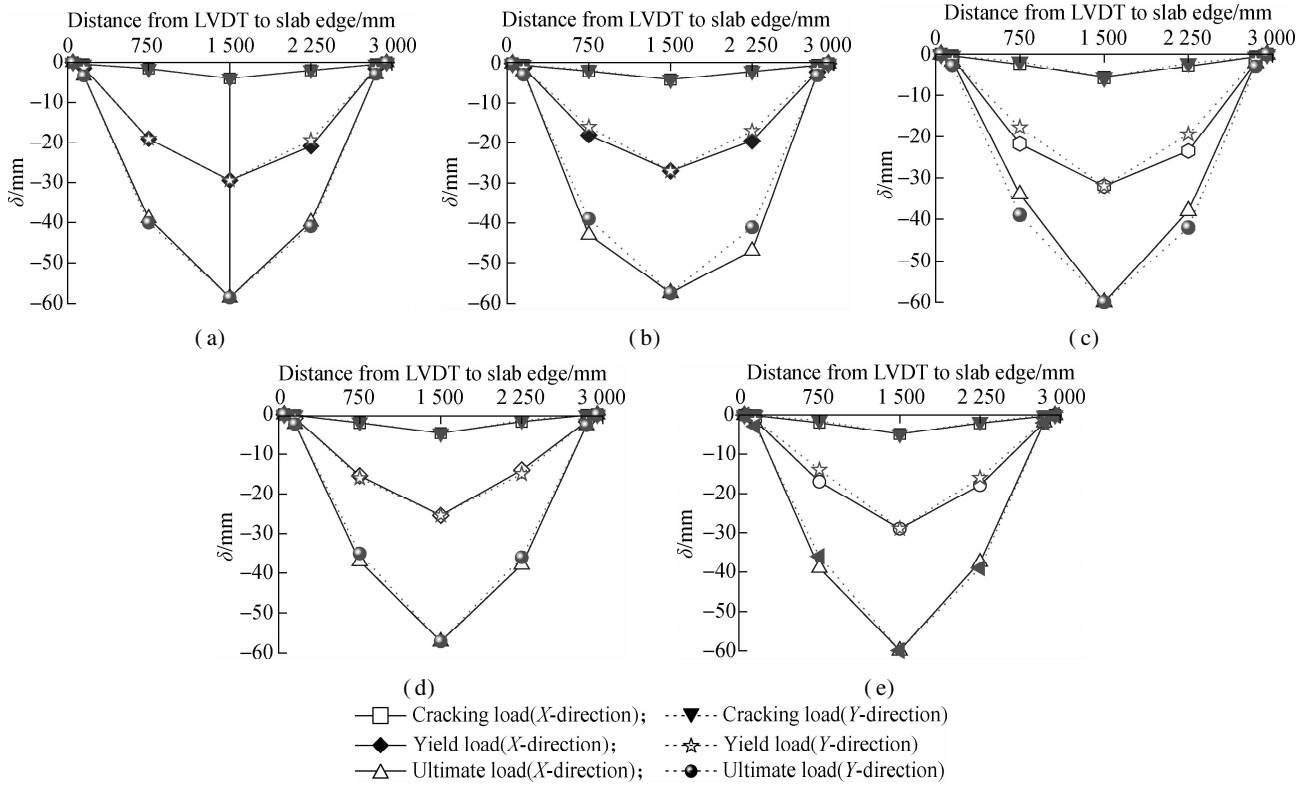

Fig. 9 Comparison of load-deflection curves at mid-span. (a) S1; (b) S2; (c) S3; (d) S4; (e) S5

each characteristic load, revealing the similarity in bending deformation between the four CCSs and the cast-in-situ concrete slab. Furthermore, the bending stiffness of the specimens decreased under the continuous cracking at the bottom centre, producing obvious inflection points in the curves under yield load and ultimate load.

2) S2 vs. S3. The vertical displacements of the two specimens were similar at cracking load, but different under the yielding load value and ultimate load value. The load-deflection curves of the two specimens were basically the same in the *X*- or *Y*-direction throughout the loading process. As a result, the base plate material only affects the deflection of the CCSs under a vertical load, but does not affect the stiffness distribution of the slabs in either direction.

3) S3 vs. S4 vs. S5. The load-deflection curves of S3 and S5 started to differ in the *X*- or *Y*- direction after cracking, which signifies the gradual change of bi-directional stress state of the two specimens, and the difference increased with the load. These phenomena can be explained by the property of the orthogonal anisotropic reinforcement slab in Ref. [25]. This property also explains the wider distribution of cracks in the *X*-direction than the *Y*-direction at the mid-span of the slab when the specimens were ultimately destroyed in Section 2.1.

2.4 Bar strain

The mid-span load-strain (F-ε) curves of compressive bars at measuring X_5 and Y_5 in Fig. 4(b) are displayed in Fig. 10.

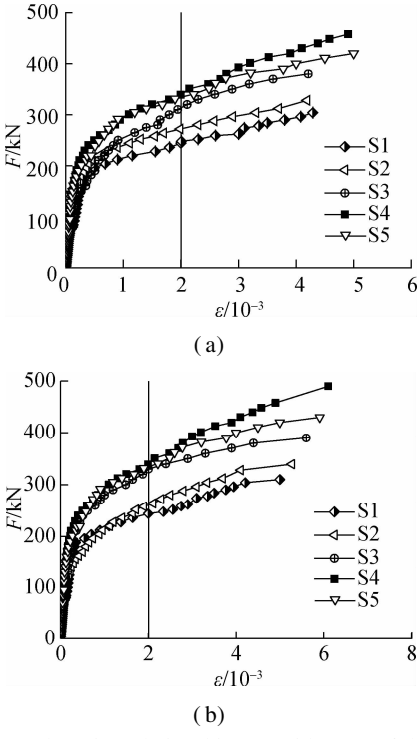

Fig. 10 Load-strain relationship at mid-span of longitudinal load-bearing reinforcements. (a) *X*-direction; (b) *Y*-direction

1) S1 vs. S2 to S5. For all specimens, each load-bar strain curve consists of three segments: the straight segment before concrete cracking, the curved segment from cracking to bar yielding, and the smooth segment from bar yielding to the ultimate state.

2) S2 vs. S3. The load-bar strain curves of both specimens coincided with each other and increased proportionally before the concrete cracked. As the cracking continued to intensify, the strain of S3 fell below that of S2 under the same load level. The probable reason lies in that the load on the tensile zone of S2 was completely carried by the tensile bars after concrete cracking; by contrast, the steel fibres of S3 carried part of the tensile stress on the cracks and strengthened the bottom bars' tensile strength.

3) S3 vs. S4 vs. S5. Under the same load level, the strain of S4 in *X*/*Y*-direction is much smaller than that of S3 or S5, because the load on the compressive bars in S4 was partially carried by the steel bar truss.

S4 was cited as an example to further illustrate the load-strain (F-ε) features of steel bar truss. The load-bar strain curve of this specimen was drawn according to the data recorded by the strain gauges of top/bottom chords and web members of truss reinforcement, which were arranged in *X* and *Y* directions, respectively. As shown in Fig. 11, the bottom chords in both directions were subjected to tensile stress, and the strain reached the yield strain of bars when the specimen entered the failure phase. The web members and the top chords of the steel bar truss were also involved in load bearing. With the increase in load, the neutral surface of the specimen moved upward continuously. The stresses of the *X*-direction upper chord, web rod and *Y*-direction web rod all shifted from compressive stress to tensile stress. It can be seen that the steel bar truss participated in the load bearing process, creating a reinforcement belt in the slab similar to that described in Ref. [33], which enhances the bearing capacity of the specimen.

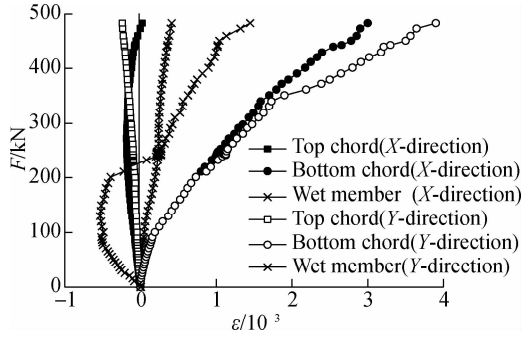

Fig. 11 Load-strain relationship at the mid-span of longitudinal load-bearing reinforcements

2.5 Load-slip curves

The load-slip (F-Δ) curves were plotted according to the two LVDTs placed at both ends of the specimens

(i.e. W10 and W11). As shown in Fig. 12, the load-slip curves reflect the good performance of the specimens under top compression and bottom tension. Considering that the connecting interface had no horizontal crack in the loading process (see Fig. 3(a)), it is safe to say that our specimens performed well under the two forces throughout the loading process.

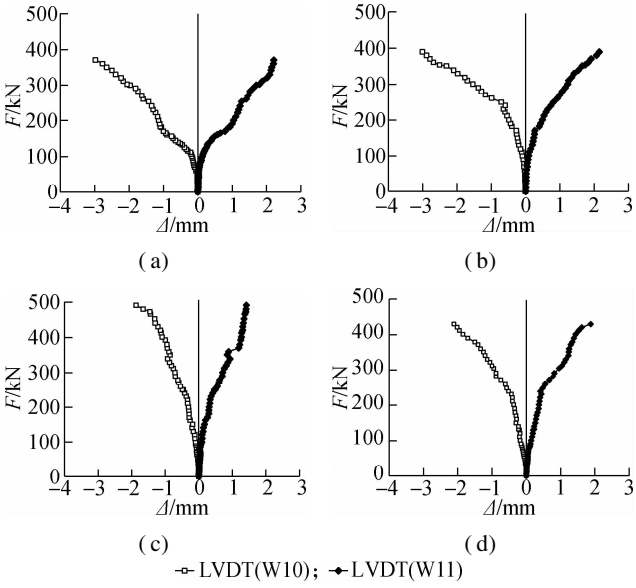

Fig. 12 Load-slip profiles at both wythes for S2 to S5. (a) S2; (b) S3; (c) S4; (d) S5

3 Flexural Capacity Analysis

3.1 Failure modes and crack pattern

As the failure mode of the CSSs is similar to that of cast-in-situ concrete slab, the bearing capacities of the four CSSs were computed using the plastic yield lines of rigid-plastic theory[34]. Whereas the base plate material and shape were proved to be the influencing factors of the ultimate bearing capacity and failure mode, the following assumptions were put forward for the calculation of ultimate bearing capacity.

1) Influence of base plate material. The contribution of steel fibres to bending bearing capacity was considered for S3 to S5, following the method in the Chinese technical specification CECS38: 2004[35]. In other words, the tensile zone at specimen bottom was treated as an equivalent rectangular stress zone.

2) Influence of steel bar truss. The analysis in Section 2.4 shows that the top chords and web members can bear fewer loads than the bottom chords. For simplicity, the load bearing capacity of the bottom chords was considered while ignoring that of the top chords or web members. The bottom chords were counted into the calculation area of the tensile bars.

3) Influence of the base plate shape. The ultimate bearing capacity of S4 (see Fig. 13(a)) was calculated according to the classical plastic yield lines of the bi-directional slabs simply-supported on four sides. Considering the difference between base plates of different shapes in the *X*- and *Y*-directions, the ultimate bearing capacities of S2, S3 and S5 were computed according to the failure mode of the orthotropic reinforcement slab (see Fig. 13(b)).

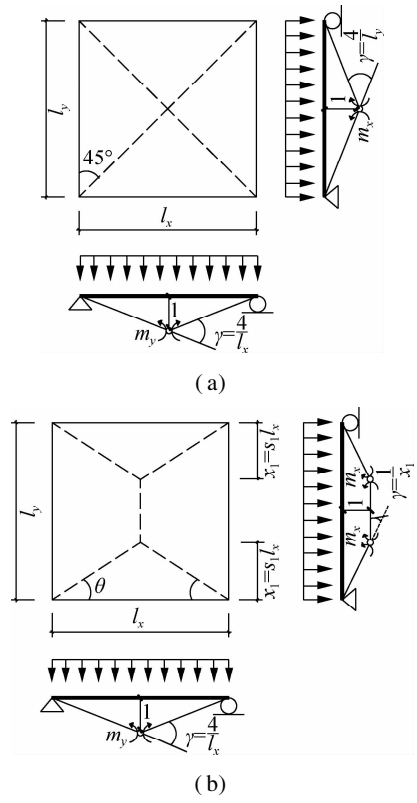

Fig. 13 Ultimate bending moment calculation model. (a) S4; (b) S2, S3 and S5

3.2 Calculation method for S2, S3 and S5

The failure mode in Fig. 13(b) shows that the plastic yield line position of the three specimens under uniform load can be determined by the values of θ (angle between the plastic hinge line and *X*-direction) or s (see Fig. 13(b)). Let m_x and m_y be the ultimate bending moments per metre of the slab in the *X*- and *Y*-directions, respectively. Then, the relationship between the mid-span ultimate bending moment in the *X*-direction and that in the *Y*-direction can be expressed as $m_x = \alpha m_y$.

Based on the theory of virtual work, when the failure occurs under the uniform ultimate load q_u, the mid-span virtual displacement of the specimen is one, and the virtual displacements at any other points are $\omega(x, y)$, and the work done by the external force equals that by the internal force.

The external work done by the ultimate uniform load q_u can be expressed as

$$W_e = q\sum_n \iint_{A_n} \omega(x, y)\ \mathrm{d}A_n = q\left(\frac{l_y}{2}l_x - \frac{l_y}{6}2sl_y\right) = \frac{ql_y^2}{6}(3n - 2s) \qquad (2)$$

The work done by the internal force on each plastic yield line can be expressed as

$$W_i = \sum m_i l_i \gamma_i = \left(m_x l_y \times \frac{4}{l_x} + m_y l_x \frac{2}{x} \right) = \left(4n + \frac{2a}{s} \right) m_y \tag{3}$$

As $W_e = W_i$, we have

$$q_u = \frac{12 m_y}{l_y^2} \frac{2n + a/s}{3n - 2s} \tag{4}$$

where $n = l_x / l_y$; $\alpha = m_y / m_x$ is the ratio of the ultimate internal moment per unit length of the plastic hinge line perpendicular to the two principal axes of the specimen.

According to the upper bound theory for rigid-plastic analysis, the position of the most dangerous plastic yield line can be obtained by the minimum uniform ultimate load. Therefore, the value of s can be deduced from $\frac{dq_u}{ds} = 0$ ($n = 1$) as

$$s = \frac{a}{2} \left(\sqrt{1 + \frac{3}{a}} - 1 \right) \tag{5}$$

Then, $\theta = \arctan(2s)$ can be drawn from the failure mode in Fig. 13(b). It can be seen from Eq. (5) that s or θ can be obtained from the failure mode when the value of α is known. Depending on the materials, the calculation of ultimate bending moments of S2, S3 and S5 is divided into two cases.

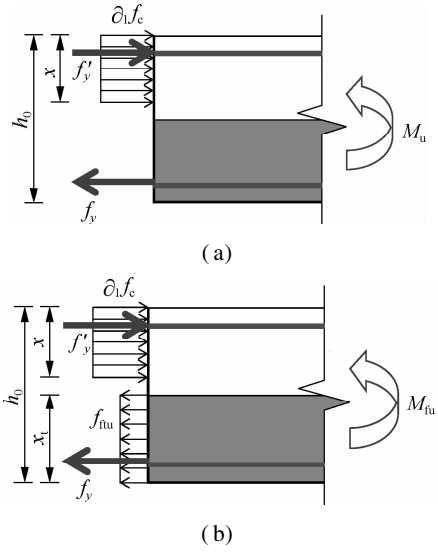

Fig. 14 Positive cross section in the *X*-/*Y*-direction calculation model. (a) S2; (b) S3, S4 and S5

Case 1 For S3 and S5, the calculation method is illustrated in Fig. 14(b). m_x and m_y are calculated by

$$\left.\begin{aligned} m_x &= A_{sx} f_y \left(h_{0x} - \frac{x_x}{2} \right) + f_{ftu} b_x x_{tx} \left(h - \frac{x_x}{2} - \frac{x_{tx}}{2} \right) \\ m_y &= A_{sy} f_y \left(h_{0x} - \frac{x_y}{2} \right) + A_{sty} f_y \left(h_{0y} - \frac{x_y}{2} \right) + \\ & \quad f_{ftu} b_y x_{ty} \left(h - \frac{x_y}{2} - \frac{x_{ty}}{2} \right) \end{aligned}\right\} \tag{6}$$

where A_{sx} is the area of bar per unit width in the *X*-direction; A_{sy} is the area of bar per unit width in the *Y*-direction; f_y is the longitudinal load-bearing bars tensile strength (the test value); h_{0x} and h_{0y} are the effective heights of cross-section; b_x, $b_y = 1\,000$ mm; x_x and x_y are the heights of the concrete compression zone in the *X*/*Y*-direction, respectively; x_x and x_y are the heights of the equivalent rectangular stress in the tensile zone; f_{ftu} is the tensile strength of the equivalent rectangle stress pattern of SFRRAC in the tension zone at the ultimate capacity state, and this value is calculated by formula $f_{ftu} = f_1 \beta_{tu} \lambda_f$.

Case 2 For S4, the calculation method is illustrated in Fig. 14(b). m_x and m_y are calculated by

$$\left.\begin{aligned} m_x &= A_{sx} f_y b_x \left(h_{0x} - \frac{x_x}{2} \right) + A_{stx} f_y b_x \left(h_{0y} - \frac{x_x}{2} \right) + \\ & \quad f_{ftu} b_x x_{tx} \left(h - \frac{x_x}{2} - \frac{x_{tx}}{2} \right) \\ m_y &= A_{sy} f_y b_y \left(h_{0y} - \frac{x_y}{2} \right) + A_{sty} f_y b_y \left(h_{0y} - \frac{x_y}{2} \right) + \\ & \quad f_{ftu} b_y x_{ty} \left(h - \frac{x_y}{2} - \frac{x_{ty}}{2} \right) \end{aligned}\right\} \tag{7}$$

where A_{stx} and A_{sty} are the areas of steel bar truss with bottom chord (*X*- or *Y*-direction) in unit slab width.

Case 3 For S2, the calculation method is illustrated in Fig. 14(a). m_x and m_y are calculated by[25]

$$\left.\begin{aligned} m_x &= A_{sx} f_y \left(h_{0x} - \frac{x_x}{2} \right) \\ m_y &= A_{sy} f_y \left(h_{0x} - \frac{x_y}{2} \right) + A_{sty} f_y \left(h_{0y} - \frac{x_y}{2} \right) \end{aligned}\right\} \tag{8}$$

Through the above methods, the θ values of S2, S3 and S5 were calculated as 40.16°, 42.23° and 42.23°, respectively. Then, the ultimate bearing capacity q_u of each specimen can be obtained by Eq. (4).

3.3 Comparative analysis

Tab. 5 lists the calculated ultimate uniform load $q_{u,c}$ and the measured ultimate uniform load $q_{u,t}$. It can be seen that the calculated ultimate bending moments of the four CCSs specimens were basically consistent with the measured results. Except for S3, the relative errors of other specimens were controlled within 10%, indicating that the previous assumptions are valid. The authors believe that the reason for the large error of S3 may be the uneven mixing of steel fibers during the production of the prefabricated bottom plate. The results need to be further studied.

Tab. 5 Calculated and measured ultimate uniform loads

No.	$q_{u,c}$ ($q_{fu,c}$) / (kN·m^{-2})	$q_{u,t}$ / (kN·m^{-2})	Relative error/%
S2	51.92	47.11	8.30
S3	56.33	46.89	16.76
S4	60.81	57.78	4.98
S5	56.33	52.22	7.30

4 Conclusions

1) From loading to failure, the specimens with the SFRRAC base plate all went through the pre-cracking, cracking and failure phases. No horizontal slippage or destruction was observed on the connecting interface. The failure process of these specimens is similar to the specimen with the concrete base plate and that with a base plate recommended by the Chinese national standard. When the precast base plates are of similar structures, the SFRRAC CCS has a similar cracking load as the ordinary CCS, and a greater ultimate load than the latter.

2) The shape of the base plate has a major impact on the bearing capacity of the CCS. When a CCS is subjected to load in two directions, the bearing capacity can be effectively enhanced by adding reinforced interfaces, especially steel bar truss, in the *X*- and *Y*-directions. According to the experimental results, the reinforcement modes can be ranked as follows by the contribution to the enhancement of bearing capacity: steel bar truss in both directions, steel bar truss in the *Y*-direction and rectangular rib in the *X*-direction, and steel bar truss in a single direction.

3) The ultimate bearing capacity of the CCS should be calculated considering the effect of the base plate shape. In particular, the impact of plate shape on plastic yield line position should be taken into account during the calculation of the ultimate bearing capacity by the plastic yield line theory when the base plate has different shapes in the *X*- and *Y*-directions.

References

[1] Cao X Y, Li Z F, Liu S. Study on factors that inhibit the promotion of SI housing system in China[J]. *Energy and Buildings*, 2015, **88**: 384 - 394. DOI:10.1016/j.enbuild.2014.11.064.

[2] Industry Handbook Committee. *PCI design handbook: Precast and prestressed concrete* [M]. 6th ed. Chicago, IL, USA: PCI, 2016: 5 - 30.

[3] Yee A A. Social and environmental benefits of precast concrete technology[J]. *PCI Journal*, 2001, **46**(3): 14 - 19. DOI:10.15554/pcij.05012001.14.19.

[4] Yee A A, Hon D. Structural and economic benefits of precast/prestressed concrete construction[J]. *PCI Journal*, 2001, **46**(4): 34 - 42. DOI: 10.15554/pcij.07012001.34.42.

[5] Mohammed B S. Structural behavior and *m-k* value of composite slab utilizing concrete containing crumb rubber [J]. *Construction and Building Materials*, 2010, **24**(7): 1214 - 1221. DOI:10.1016/j.conbuildmat.2009.12.018.

[6] Holmes N, Dunne K, O'Donnell J. Longitudinal shear resistance of composite slabs containing crumb rubber in concrete toppings[J]. *Construction and Building Materials*, 2014, **55**: 365 - 378. DOI:10.1016/j.conbuildmat.2014.01.046.

[7] Majdi Y, Hsu C T T, Zarei M. Finite element analysis of new composite floors having cold-formed steel and concrete slab[J]. *Engineering Structures*, 2014, **77**: 65 - 83. DOI:10.1016/j.engstruct.2014.07.030.

[8] An Q, Ren Q Y, Liu H B, et al. Dynamic performance characteristics of an innovative cable supported beam structure-concrete slab composite floor system under human-induced loads [J]. *Engineering Structures*, 2016, **117**: 40 - 57. DOI:10.1016/j.engstruct.2016.02.038.

[9] Kim H Y, Jeong Y J. Ultimate strength of a steel-concrete composite bridge deck slab with profiled sheeting [J]. *Engineering Structures*, 2010, **32**(2): 534 - 546. DOI:10.1016/j.engstruct.2009.10.014.

[10] Ueda T, Stitmannaithum B. Shear strength of precast prestressed hollow slabs with concrete topping [J]. *ACI Structural Journal*, 1991, **88**(4): 402 - 410. DOI:10.14359/2694.

[11] Ibrahim I S, Elliott K S, Abdullah R, et al. Experimental study on the shear behaviour of precast concrete hollow core slabs with concrete topping[J]. *Engineering Structures*, 2016, **125**: 80 - 90. DOI:10.1016/j.engstruct.2016.06.005.

[12] Thanoon W A, Yardim Y, Jaafar M S, et al. Structural behaviour of ferrocement-brick composite floor slab panel [J]. *Construction and Building Materials*, 2010, **24**(11): 2224 - 2230. DOI:10.1016/j.conbuildmat.2010.04.034.

[13] Carbonari G, Cavalaro S H P, Cansario M M, et al. Flexural behaviour of light-weight sandwich panels composed by concrete and EPS[J]. *Construction and Building Materials*, 2012, **35**: 792 - 799. DOI:10.1016/j.conbuildmat.2012.04.080.

[14] Mohamad N, Khalifa H, Abdul Samad A A, et al. Structural performance of recycled aggregate in CSP slab subjected to flexure load[J]. *Construction and Building Materials*, 2016, **115**: 669 - 680. DOI:10.1016/j.conbuildmat.2016.04.086.

[15] Prabakar J, Alagusundaramoorthy P. Precast concrete sandwich one-way slabs under flexural loading[J]. *Engineering Structures*, 2017, **138**: 447 - 457. DOI: 10.1016/j.engstruct.2017.02.033.

[16] Benayoune A, Samad A A A, Trikha D N, et al. Flexural behaviour of pre-cast concrete sandwich composite panel—Experimental and theoretical investigations[J]. *Construction and Building Materials*, 2008, **22**(4): 580 - 592. DOI:10.1016/j.conbuildmat.2006.11.023.

[17] Kim S W, Yun H D. Influence of recycled coarse aggregates on the bond behavior of deformed bars in concrete [J]. *Engineering Structures*, 2013, **48**: 133 - 143. DOI: 10.1016/j.engstruct.2012.10.009.

[18] Dulsang N, Kasemsiri P, Posi P, et al. Characterization of an environment friendly lightweight concrete containing ethyl vinyl acetate waste[J]. *Materials & Design*, 2016, **96**: 350 - 356. DOI:10.1016/j.matdes.2016.02.037.

[19] Etxeberria M, Vázquez E, Marí A, et al. Influence of amount of recycled coarse aggregates and production process on properties of recycled aggregate concrete[J]. *Cement and Concrete Research*, 2007, **37**(5): 735 - 742. DOI:10.1016/j.cemconres.2007.02.002.

[20] Dong K L. *Research on basic mechanical performance of fiber recycled recycled aggregate concrete* [D]. Xi'an: Xi'an University of Architecture and Technology, 2015.

(in Chinese)
[21] Ministry of Housing and Urban-Rural Development of the People's Republic of China. Technical specification for precast concrete structures: JGJ 1—2014 [S]. Beijing: China Architecture and Building Press, 2014. (in Chinese)
[22] Ministry of Housing and Urban-rural development of the People's Republic of China. Code for seismic design of buildings: GB 50011—2015 [S]. Beijing: China Architecture and Building Press, 2015. (in Chinese)
[23] Ministry of Housing and Urban-rural development of the People's Republic of China. Standard for test method of concrete structures: GB/T 50152—2012 [S]. Beijing: China Architecture and Building Press, 2012. (in Chinese)
[24] Feng P, Cheng S, Bai Y, et al. Mechanical behavior of concrete-filled square steel tube with FRP-confined concrete core subjected to axial compression [J]. *Composite Structures*, 2015, **123**: 312 - 324. DOI: 10. 1016/j. compstruct. 2014. 12. 053.
[25] Park R, Gambe W L. *Reinforced concrete slab* [M]. Translated by Huang G Z, Cheng Y H. Shanghai: Tongji University Press, 1992: 174 - 184. (in Chinese)
[26] Prisco M, Plizzari G, Vandewalle L. Fibre reinforced concrete: New design perspectives [J]. *Materials and Structures*, 2009, **42**(9): 1261 - 1281. DOI: 10. 1617/s11527-009 - 9529-4.
[27] Ministry of Housing and Urban-rural development of the People's Republic of China. Load code for the design of building structures: GB 50009—2012 [S]. Beijing: China Architecture and Building Press, 2012. (in Chinese)
[28] Тимошенко S, Woinowsky K S. *Theory of plates and shells* [M]. 2nd ed. Translated by Translation Group of Theory of Plates and Shells. Beijing: China Science Press, 1977: 189 - 220. (in Chinese)
[29] Rahimi Mansour F, Abu Bakar S, Ibrahim I S, et al. Flexural performance of a precast concrete slab with steel fiber concrete topping [J]. *Construction and Building Materials*, 2015, **75**: 112 - 120. DOI: 10. 1016/j. conbuildmat. 2014. 09. 112.
[30] Zhang J S, Yao Y, Zhou X H, et al. Failure mode and ultimate bearing capacity of precast ribbed panels used for concrete composite slabs [J]. *Advances in Structural Engineering*, 2013, **16**(12): 2005 - 2017. DOI: 10. 1260/1369-4332. 16. 12. 2005.
[31] Cao W L, Zhang J, Dong H Y, et al. Experimental research on flexural performance of high strength recycled aggregate concrete slabs with steel bar truss [J]. *Journal of Building Structures*, 2014, **35**(10): 31 - 38. DOI: 10. 14006/j. jzjgxb. 2014. 10. 004. (in Chinese)
[32] Yang Y, Liu R Y, Huo X D, et al. Static experiment on mechanical behavior of innovative flat steel plate-concrete composite slabs [J]. *International Journal of Steel Structures*, 2018, **18**(2): 473 - 485. DOI: 10. 1007/s13296-018 - 0012-3.
[33] Meisami M H, Mostofinejad D, Nakamura H. Strengthening of flat slabs with FRP fan for punching shear [J]. *Composite Structures*, 2015, **119**: 305 - 314. DOI: 10. 1016/j. compstruct. 2014. 08. 041.
[34] Xu B Y, Liu X S. *Plastic ultimate analysis of structures* [M]. Beijing: China Architecture and Building Press, 209 - 245. (in Chinese)
[35] China Association for Engineering Construction Standardization. Technical specification for fiber reinforced concrete structures: CECS38: 2004 [S]. Beijing: China Planning Press, 2004. (in Chinese)

不同构造形式钢纤维增强再生混凝土双向叠合板受弯性能

罗 斌[1] 黄 炜[2]

([1] 兰州理工大学土木工程学院, 兰州 730050)
([2] 西安建筑科技大学土木工程学院, 西安 710055)

摘要: 为推动绿色再生类材料在叠合楼板中的应用, 研究不同构造形式所组成的混凝土叠合板受弯性能异同, 开展了 3 块钢纤维增强再生混凝土双向叠合板、1 块普通现浇混凝土双向板及 1 块《装配式混凝土结构技术规程》推荐的普通混凝土桁架钢筋双向叠合板的抗弯性能静载对比试验. 分别从破坏形态、荷载-挠度曲线、荷载-钢筋应变曲线、荷载-滑移曲线、裂缝分布规律对试件的承载能力、受弯性能及双向受力性能等方面进行了系统分析. 研究结果表明: 钢纤维增强钢纤维再生混凝土叠合板与普通混凝土叠合板及普通现浇混凝土板的弯曲破坏过程相似, 均经历了弹塑性阶段、塑性阶段和破坏阶段, 裂缝、挠度发展均较充分, 且未有突然断裂或沿叠合面出现水平裂缝等破坏现象; 同时, 不同的预制底板构造形式对钢纤维增强再生混凝土叠合楼板的受弯性能有较大影响, 在用塑性屈服线理论计算极限承载力时, 应考虑不同预制底板形式对塑性屈服线位置的影响.

关键词: 混凝土叠合板; 构造形式; 钢筋桁架; 受弯性能; 极限承载力
中图分类号: TU375. 2